AIAA 2002-0078
Effects of Endwall Geometry and Stacking on Two-Stage Supersonic Turbine Performance

Daniel J. Dorney, Lisa W. Griffin
NASA Marshall Space Flight Center
MSFC, AL

Frank W. Huber
Riverbend Design Services
Palm Beach Gardens, FL

Douglas L. Sondak
Boston University
Boston, MA

40th Aerospace Sciences Meeting & Exhibit
14-17 January 2002 / Reno, NV

EFFECTS OF ENDWALL GEOMETRY AND STACKING ON TWO-STAGE SUPERSONIC TURBINE PERFORMANCE

Daniel J. Dorney* **Lisa W. Griffin†**
Fluids Dynamics Analysis Branch
NASA Marshall Space Flight Center
Marshall Space Flight Center, Alabama, USA

Frank W. Huber‡
Riverbend Design Services
Palm Beach Gardens, Florida, USA

Douglas L. Sondak§
Office of Information Technology
Boston University
Boston, MA, USA

ABSTRACT

The drive towards high-work turbines has led to designs which can be compact, transonic, supersonic, counter rotating, or use a dense drive gas. These aggressive designs can lead to strong secondary flows and airfoil flow separation. In many cases the secondary and separated flows can be minimized by contouring the hub/shroud endwalls and/or modifying the airfoil stacking. In this study, three-dimensional unsteady Navier-Stokes simulations were performed to study three different endwall shapes between the first-stage vanes and rotors, as well as two different stackings for the first-stage vanes. The predicted results indicate that changing the stacking of the first-stage vanes can significantly impact endwall separation (and turbine performance) in regions where the endwall profile changes.

*Aerospace Engineer, Senior Member AIAA.
†Team Leader, Senior Member AIAA.
‡President, Senior member AIAA.
§Senior Scientific Programmer, Senior Member AIAA.

NOMENCLATURE

C	- Axial chord
f	- Frequency
M	- Mach number
P	- Static pressure
r	- Radius
ΔP	- Amplitude of pressure variation
$\tilde{r}$	- $(r - r_{hub})/(r_{tip} - r_{hub})$
T	- Static temperature
W	- Work

GREEK SYMBOLS

β	- Relative circumferential angle
η	- Efficiency
γ	- ratio of specific heats
ρ	- Density
Ω	- Rotor rotational speed

SUBSCRIPTS

in	- Inlet
out	- Outlet
t	- Stagnation quantity, time derivative
ts	- Total-to-static
tt	- Total-to-total

0 - Vane-1 inlet
4 - Rotor-2 exit
1/2 - Half-amplitude
∞ - Free stream

INTRODUCTION

Modern high-work turbines can be compact, transonic, supersonic, counter rotating, or uses a dense drive gas. The vast majority of modern rocket turbine designs fall into these categories. These turbines are often characterized by large amounts of flow unsteadiness. The flow unsteadiness can have a major impact on the turbine performance and durability. For example, the Space Transportation Main Engine (STME) fuel turbine, a high-work transonic design, was found to have an unsteady interrow shock which reduced efficiency by 2 points and increased dynamic loading by 24 percent. The Revolutionary Reusable Technology Turbopump (RRTT), which uses full flow oxygen for its drive gas, was found to shed vortices with such energy as to raise serious blade durability concerns. In both cases, the sources of the problems were uncovered (before turbopump testing) with the application of validated, unsteady computational fluid dynamics (CFD) to the designs. In the case of the RRTT and the Alternate Turbopump Development (ATD) turbines, the unsteady CFD codes were used not just to identify problems, but to guide designs which mitigate problems due to unsteadiness. Using unsteady flow analyses as a part of the design process has led to turbine designs with higher performance (which effects temperature and mass flow rate) and fewer dynamics problems. The works of Griffin *et al.* [1]-[4], Garcia *et al.* [5] and Griffin and Dorney [6] are examples of the application of unsteady CFD to rocket turbine designs.

More recently, CFD has been used to design a two-stage supersonic turbine which will be tested experimentally during 2002 [7]-[9]. Numerical simulations (including meanline, two-dimensional CFD and three-dimensional CFD analyses in conjunction with optimization techniques) were used to design both the flowpath and the airfoil geometries. During the course of this work a large separated flow region was detected on the hub endwall between the first-stage vane and the first-stage rotor.

Two methods used are normally to control the secondary/separated flows (and associated losses) in supersonic turbines: endwall contouring and airfoil stacking. In the current investigation the flow path between the first-stage vanes and rotors, and the stacking of the first-stage vanes, were varied in an effort to improve turbine performance. The geometric variations have been studied by performing a series of unsteady three-dimensional numerical simulations for the two-stage turbine.

NUMERICAL ALGORITHM

The governing equations considered in this study are the time dependent, three-dimensional Reynolds-averaged Navier-Stokes equations. To extend the equations of motion to turbulent flows, an eddy viscosity formulation is used. The turbulent viscosity is calculated using the two-layer Baldwin-Lomax algebraic turbulence model [10].

The numerical algorithm used in the three-dimensional computational procedure consists of a time-marching, implicit, finite-difference scheme. The procedure is third-order spatially accurate and second-order temporally accurate. The inviscid fluxes are discretized according to the scheme developed by Roe [11]. The viscous fluxes are calculated using standard central differences. An approximate-factorization technique is used to compute the time rate changes in the primary variables. Newton subiterations are used at each global time step to increase stability and reduce linearization errors. For all cases investigated in this study, two Newton subiterations were performed at each time step. Message Passing Interface (MPI) and OpenMP software have been implemented into the numerical analysis to reduce the computation time for large-scale three-dimensional simulations.

The Navier-Stokes analysis uses O- and H-type zonal grids to discretize the flow field and facilitate relative motion of the rotating components (see Fig. 1). The O-grids are body-fitted to the surfaces of the airfoils and generated using an elliptic equation solution procedure. They are used to properly resolve the viscous flow in the blade passages and to easily apply the algebraic turbulence model. The algebraically-generated H-grids are used to discretize the remainder of the flow field.

The computational analysis has been validated on several supersonic turbine geometries (*e.g.*, Refs. [6], [12], [13]).

BOUNDARY CONDITIONS

The theory of characteristics is used to determine the boundary conditions at the inlet and exit of the computational domain. For subsonic inlet flow four quantities are specified and one is extrapolated from

the interior of the computational domain. In particular, the total pressure, total temperature, and the circumferential and radial flow angles are specified as a function of the radius. The upstream running Riemann invariant is extrapolated from the interior of the computational domain.

For subsonic outflow one flow quantity is specified and four are extrapolated from the interior of the computational domain. The circumferential and radial flow angles, total pressure, and the total temperature are extrapolated from the interior of the computational domain. The pressure ratio, P_4/P_{t0} is specified at mid-span of the computational exit and the pressure at all other radial locations at the exit is obtained by integrating the equation for radial equilibrium. For supersonic outflow all the flow variables are extrapolated. Periodicity is enforced along the outer boundaries of the H-grids in the circumferential direction.

For viscous simulations, no-slip boundary conditions are enforced along the solid surfaces. It is assumed that the normal derivative of the pressure is zero at solid wall surfaces. In addition, a specified heat flux distribution is held constant in time along the solid surfaces.

The flow variables at zonal boundaries are explicitly updated after each time step by interpolating values from the adjacent grid.

GEOMETRY AND GRIDS

The two-stage supersonic turbine configuration, typical of those proposed for a reusable launch vehicle, has 12 first-stage vanes, 30 first-stage rotors, 73 second-stage vanes and 56 second-stage rotors. In the current effort, a 15-vane/30-rotor/75-vane/60-rotor (1/2/5/4) airfoil approximation has been made. To keep the pitch-to-chord ratio (blockage) constant, the first-stage vanes were scaled by a factor of 12/15, the second-stage vanes were scaled by a factor of 73/75 and the second-stage rotors were scaled by a factor of 56/60. The tip clearance in the first- and second-stage rotors was set at the design value of approximately 2.0% of the respective rotor heights.

The grid densities (number of passages×i×j×k) for the turbine simulations are presented in Table 1. The total number of grid points used to discretize the turbine was 4,139,957. Figure 1 illustrates an $(x-y)$ view of the grids at midspan, where every other grid point in each coordinate direction has been removed for clarity. Figure 2 illustrates the grids used to discretize the clearance region of the second-stage rotor. Figure 3 shows a perspective view of the two-stage turbine. The average value of y^+, the non-dimensional distance of the first grid line above the surface was approximately 1.0 for the airfoils surfaces and 1.5 for the endwall surfaces.

The simulations were run on 24 (400 MHz) processors of an SGI Origin2000. Each simulation was run for 15.0 global cycles (one complete rotor revolution) at 22,000 iterations per cycle. A global cycle is defined as the time it takes for the two first-stage rotor blades to pass by the first-stage vane airfoil. The value of 22,000 iterations per cycle was chosen to resolve all the (expected) frequencies of interest. Each iteration required approximately 9.0 seconds computation time on 24 processors. The time periodicity of the solutions was determined by interrogating pressure traces at different points along the airfoil surfaces.

NUMERICAL RESULTS

The two-stage turbine under consideration has a design inlet Mach number of $M_0 = 0.08$, an inlet static pressure of 2225 *psia*, and an inlet static temperature of approximately $T_0 = 2225\ R$. The rotor rotates at $\Omega = 31,343$ RPM, the Reynolds number (based on the inlet conditions and the rotor axial chord) is approximately 1.2×10^6 and the ratio of the rotor exit static pressure to vane inlet total pressure is $P_4/P_{t0} = 0.1135$. The operating fluid is hydrogen-rich steam and the average ratio of specific heats is $\gamma = 1.3538$.

Four different simulations have been performed to determine the effects of endwall shape and first-stage vane stacking on the performance of the two-stage turbine.

1. Case 1 - The radius of the inner diameter (ID) and outer diameter (OD) are transitioned from the nominal values in the first-stage vane passage to the final values in the rotor passage beginning three-quarters of the way between the vane trailing edge and concluding at the rotor leading edge (see Fig. 4). Case 1 represents the original turbine geometry based on previous work [7]-[9].

2. Case 2 - The radius of the ID and OD are transitioned from the nominal values in the vane passage to the final values in the rotor passage beginning at the vane trailing edge and concluding at the rotor leading edge (see Fig. 4).

3. Case 3 - The radius of the inner diameter (ID)

is kept constant at the value used in the rotor. The radius of the OD is transitioned from the nominal value in the vane passage to the final value in the rotor passage beginning at the vane trailing edge and concluding at the rotor leading edge (see Fig. 4). Note, in this case the height of the vane was increased to keep the vane flow area the same as in Cases 1 and 2.

4. Case 4 - The flow path is identical to that used in Case 3. The vane airfoils are stacked along the trailing edge instead of the center of gravity (as it was in Cases 1, 2 and 3).

An overview of the turbine flow field is presented in Figs. 5 and 6, which contain instantaneous absolute Mach and entropy contours, respectively, at midspan of the turbine for Case 4. Figure 5 highlights the strong expansion and shock structures between the first-stage vane and rotors, as well as weaker shock structures near the leading and trailing edges of the second-stage vane. Figure 6 highlights flow separation on the suction surface of both rotors, which is typical of supersonic turbine flow fields.

Time-averaged entropy contours midway between the first-stage vane and rotor passages for Case 1 are shown in Fig. 7. The contours show a large region of separated flow extending from the hub to approximately 20% of the span. The axial extent of the region was confined to the area between the vane trailing edge and the rotor leading edge. It was initially theorized that the large separated flow region was being induced by the rapid expansion in the endwall flowpath in Case 1. Reducing the slope of the endwall in Cases 2 and 3, however, did not significantly affect the size of the separated flow region (see Figs. 8 and 9). The next hypothesis for the large separated flow region was that stacking the vanes along the center of gravity causes the vane throat to point outwards towards the shroud endwall, giving the flow a tendency to pull away from the hub endwall. Re-stacking the vanes along a radial line connecting the trailing edge points significantly reduced the size of the separated flow region (see Fig. 10).

Tables 2 to 5 contain the time-averaged relative-frame flow quantities at the inlet and exit of each blade row for all four cases. Some of the relevant information which can be deduced from these tables includes:

- Reducing the size of the separated flow region in Case 4 resulted in a value of the average vane exit Mach number (1.37) which is closer to the design value of 1.50.

- Reducing the size of the separated flow region in Case 4 gives a significant increase (nearly 6 points) in turbine efficiency compared to Case 1. A more detailed comparison of Cases 1 and 4 is presented below.

- The changes made to the first stage had little effect on the flow in the second stage.

The differences between the flow fields in Cases 1 and 4 are explored in more detail by comparing surface pressures and radial profiles. Figures 11 and 12 illustrate the time-averaged surface pressures on the first-stage vane and rotor, respectively, at 10%, 50% and 90% of the span. Re-stacking the vane results in the loading shifting towards the leading edge at the hub and towards the trailing edge at the tip (see Fig. 11). The vane loadings are similar at 50% of the span. There are significant differences between the rotor surface pressures in Cases 1 and 4 (see Fig. 12). At 10% span the surface pressures are much greater in Case 1 because of the low Mach number associated with the separated flow. The loading on the rotor at 10% span is also greater in the Case 1 than in Case 4. The presence of the low flow region near the hub in Case 1 forces more of the flow through the outboard regions of the rotor. The loadings at 50% and 90% span are similar in Cases 1 and 4.

An indication of the unsteadiness in the turbine can be obtained from Figs. 13-16, which show the unsteady pressure envelopes for all four blade rows at 10%, 50% and 90% of the span in Case 4. The unsteadiness on the first-stage vane, which is generated mainly by interaction with the rotor potential field and bow shock, is confined to the unconvered portion of the suction surface by the choked throat in passage (see Fig. 13). The first-stage rotor blades, as well as the airfoils in the second stage of the turbine, experience a significant amount of unsteadiness. The unsteadiness in these blade rows is generated from several sources, including interaction with the potential fields of the upstream and downstream blade rows, periodic interaction with the wakes from upstream blade rows and temporal variations in shock location and strength. The unsteadiness in all four blade rows is relatively constant as a function of the span.

Fourier decompositions of the unsteady pressure at 5% of the axial chord on the suction surface of the first-stage rotor at 10% and 50% of the span are shown in Figs. 17 and 18, respectively, for Cases 1 and 4. Note, the frequencies in Case 1 were shifted by 1 kHz to facilitate comparisons. At 10% span the

reduction in the separated flow region causes the rotor to experience more influence from the vane wake (as indicated by an increase in the unsteadiness near 8 kHz). At 50% span both cases exhibit significant unsteadiness at the vane passing frequency and twice the vane passing frequency. The higher harmonic may actually be caused by the vane trailing edge expansion fan, which is offset from the vane wake by nearly half the vane circumferential pitch.

Time-averaged radial profiles of the absolute Mach number at the exit of each blade row in Cases 1 and 4 are shown in Figs. 19-22. The Mach number profile at the exit of the first-stage vane (see Fig. 19) clearly shows the extent of the separated flow region. The flow field begins to recover by the time it exits the first-stage rotor (see Fig. 20), and the Mach number profiles are nearly identical in the second stage of the turbine (see Figs. 21 and 22). The presence of tip leakage flow is evident behind both rotor rows (see Figs. 20 and 22).

Time-averaged radial profiles of the absolute circumferential flow angle at the exit of each blade row in Cases 1 and 4 are shown in Figs. 23-26. As noted above, the large flow (and angle) deficit near the first-stage vane hub in Case 1 (see Fig. 23) causes a radial shift in the flow distribution within the rotor (see Fig. 24). Similar to the Mach number profiles, the flow angle profiles in the second stage are similar for both cases. Thus, the geomertic variations in the first-stage do not have a significant impact on the flow in the second stage.

For completeness, the time-averaged radial profiles of the absolute total pressure are shown in Figs. 27-30. As expected, the character of the total pressure profiles follows closely with that of the Mach number profiles. The large separated flow region at the exit of the first-stage vane, the redistribution of the flow in the first-stage rotor, as well as the recovery of the flow in the second stage are all visible.

CONCLUSIONS

A set of unsteady three-dimensional Navier-Stokes simulations has been used to investigate the effects of endwall shape and first-stage vane stacking on the performance of a two-stage supersonic turbine. Restacking of the vanes was successfully used to eliminate a large separated/secondary flow region at the hub between the first-stage vanes and rotors. Altering the shape of the endwall in the first stage had little effect on the separated flow region. There was a significant performance increase obtained at the design flow conditions by reducing the separated flow region. It is anticipated that the benefits of improving the behavior of the flow near the endwall will be even greater at off-design operating conditions.

ACKNOWLEDGEMENTS

The computer time for the flow simulations was provided by NASA Ames Research Center. The authors are especially grateful to Mr. Chuck Niggley for assisting with the use of the computers.

References

[1] Griffin, L. W., and Rowey, R. J., "Analytical Investigation of the Unsteady Aerodynamic Environments in Space Shuttle Main Engine (SSME) Turbines", ASME Paper No. 93-GT-363, 1993, Cincinnati, OH, June.

[2] Griffin, L. W., and Huber, F. W., "Advancement of Turbine Aerodynamic Design Techniques", ASME Paper No. 93-GT-370, Cincinnati, 1993, OH, June.

[3] Griffin, L. W., Huber, F. W., and Sharma, O. P., "Performance Improvement Through Indexing of Turbine Airfoils: Part 2: Numerical Simulation", *ASME Journal of Turbomachinery*, Vol. 118, No. 4, 1996, pp. 636-642.

[4] Griffin, L. W., and Nesman, T., "Prediction of the Unsteady Aerodymanic Environment in the RRTT Turbine", presented at the 14th Workshop for Fluid Dynamic Applications in Rocket Propulsion and Launch Vehicle Technology, NASA/Marshall Space Flight Center, April 23-25, 1996.

[5] Garcia, R., Griffin, L. W., Benjamin, T. G., Cornelison, J. W., Ruf, J. H., and Williams, R. W., "Computational Fluid Dynamics Analysis in Support of the Simplex Turbopump Design", NASA CP-3282 Vol. 1, 1995, pp. 462-470.

[6] Griffin, L. W. and Dorney, D. J., "Simulations of the Unsteady Flow Through the Fastrac Supersonic Turbine," *ASME Journal of Turbomachinery*, Vol. 122, No. 2, April, 2000, qpp. 225-233

[7] Griffin, L. W., Dorney, D. J., Huber, F. W., Tran, K., Shyy, W., and Papila, N., "Detailed Aerodynamic Design Optimization of an RLV Turbine," AIAA 2001-3397,

37th AIAA/ASME/SAE/ASEE Joint Propulsion Conference, Salt Lake City, UT, July 8-11, 2001.

[8] Papila, N., Shyy, W, Griffin, L. W., Dorney, D. J., "Shape Optimization of Supersonic Turbines Using Response Surface and Neural Network Methods," AIAA 2001-1065, 39th AIAA Aerospace Sciences Meeting and Exhibit, Reno, NV, January 8-11, 2001.

[9] Griffin, L. W., and Dorney, D. J., "RLV Turbine Performance Optimization," PERC 12th Symposium on Propulsion, Cleveland, OH, October 26-27, 2000.

[10] Baldwin, B. S., and Lomax, H., "Thin Layer Approximation and Algebraic Model for Separated Turbulent Flow," AIAA Paper 78-257, 16th AIAA Aerospace Sciences Meeting and Exhibit, Huntsville, AL, January, 1978.

[11] Roe, P. L., "Approximate Riemann Solvers, Parameter Vectors, and Difference Schemes," *Journal of Computational Physics*, Vol. 43, 1981, pp. 357-372.

[12] Dorney, D. J., Griffin, L. W., and Huber, F., "A Study of the Effects of Tip Clearance in a Supersonic Turbine," *ASME Journal of Turbomachinery*, Vol. 122, No. 4, October, 2000, pp. 674-673.

[13] Dorney, D. J., Griffin, L. W., Huber, F., and Sondak, D. L., "Unsteady Flow in a Supersonic Turbine Stage With Variable Specific Heats," AIAA Paper 2001-3884, 37th AIAA/ASME/SAE/ASEE Joint Propulsion Conference, Salt Lake City, UT, July 8-11, 2001, also accepted for publication in the *AIAA Journal of Propulsion and Power.*

Grid Type	Vane-1	Rotor-1	Vane-2	Rotor-2
O	1x141x31x51	2x151x21x51	5x121x31x51	4x121x31x51
H	1x67x41x51	2x64x41x51	5x64x41x51	4x82x41x51
Tip	–	2x151x26x7	–	4x121x16x7
Total Points	363,018	646,054	1,525,625	1,505,260

Table 1: Grid dimensions for the 2-stage turbine.

Variable	Vane-1	Rotor-1	Vane-2	Rotor-2
M_{in}	0.08	0.91	0.59	1.09
M_{out}	1.17	0.85	1.09	0.81
P_{in} (psia)	2225.	604.	564.	300.
P_{out} (psia)	604.	564.	300.	254.
Pt_{in} (psia)	2235.	1131.	721.	458.
Pt_{out} (psia)	1611.	923.	631.	411.
Tt_{in} (R)	2225.	2000.	1863.	1703.
Tt_{out} (R)	2224.	1986.	1852.	1698.
β_{in} (deg)	0.0	60.5	-57.1	56.8
β_{out} (deg)	63.8	-70.1	67.4	-55.2
W (BTU/lbm)	–	495.	–	418.
Reaction	–	0.061	–	0.161
$\eta_{tt-overall}$	–	–	–	0.621
$\eta_{ts-overall}$	–	–	–	0.564

Table 2: Turbine time-averaged flow quantities for Case 1.

Variable	Vane-1	Rotor-1	Vane-2	Rotor-2
M_{in}	0.08	0.90	0.59	1.09
M_{out}	1.15	0.86	1.09	0.80
P_{in} (psia)	2225.	611.	560.	299.
P_{out} (psia)	611.	560.	299.	254.
Pt_{in} (psia)	2235.	1124.	719.	455.
Pt_{out} (psia)	1593.	922.	626.	408.
Tt_{in} (R)	2225.	2004.	1865.	1706.
Tt_{out} (R)	2224.	1989.	1856.	1705.
β_{in} (deg)	0.0	59.2	-56.5	56.8
β_{out} (deg)	61.0	-70.7	66.9	-55.1
W (BTU/lbm)	–	502.	–	416.
Reaction	–	0.066	–	0.159
$\eta_{tt-overall}$	–	–	–	0.623
$\eta_{ts-overall}$	–	–	–	0.568

Table 3: Turbine time-averaged flow quantities for Case 2.

Variable	Vane-1	Rotor-1	Vane-2	Rotor-2
M_{in}	0.08	0.91	0.59	0.79
M_{out}	1.15	0.86	1.08	0.85
P_{in} (psia)	2225.	598.	554.	300.
P_{out} (psia)	598.	554.	300.	254.
Pt_{in} (psia)	2235.	1115.	711.	453.
Pt_{out} (psia)	1577.	922.	622.	406.
Tt_{in} (R)	2225.	2004.	1865.	1709.
Tt_{out} (R)	2224.	1989.	1857.	1704.
β_{in} (deg)	0.0	59.1	-57.3	56.7
β_{out} (deg)	60.0	-70.7	67.5	-55.3
W (BTU/lbm)	–	481.	–	425.
Reaction	–	0.059	–	0.165
$\eta_{tt-overall}$	–	–	–	0.609
$\eta_{ts-overall}$	–	–	–	0.553

Table 4: Turbine time-averaged flow quantities for Case 3.

Variable	Vane-1	Rotor-1	Vane-2	Rotor-2
M_{in}	0.08	1.07	0.59	0.80
M_{out}	1.37	0.86	1.09	0.86
P_{in} (psia)	2225.	602.	560.	300.
P_{out} (psia)	602.	560.	300.	254.
Pt_{in} (psia)	2235.	1237.	720.	454.
Pt_{out} (psia)	1835.	926.	625.	408.
Tt_{in} (R)	2225.	1996.	1863.	1707.
Tt_{out} (R)	2223.	1989.	1856.	1703.
α_{in} (deg)	0.0	72.7	-57.3	56.8
α_{out} (deg)	76.4	-69.7	67.5	-55.1
W (BTU/lbm)	–	583.	–	427.
Reaction	–	0.031	–	0.164
$\eta_{tt-overall}$	–	–	–	0.680
$\eta_{ts-overall}$	–	–	–	0.618

Table 5: Turbine time-averaged flow quantities for Case 4.

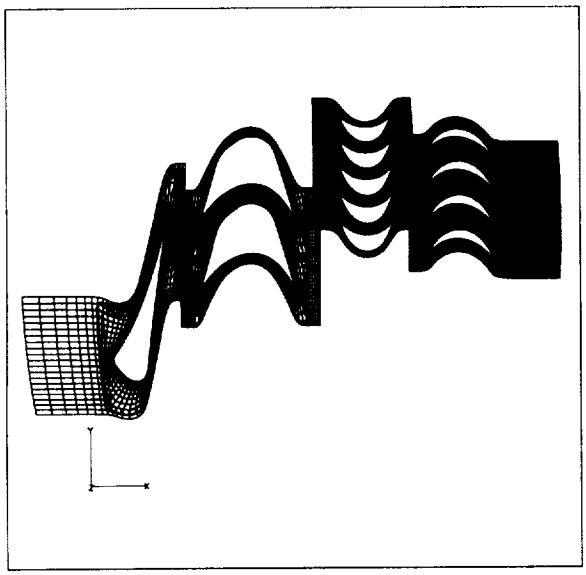

Figure 1: Radial view of the grid at midspan.

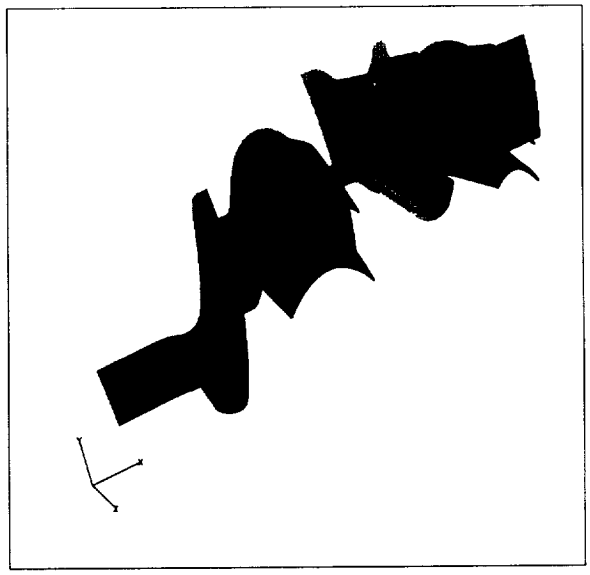

Figure 3: Perspective view of the turbine.

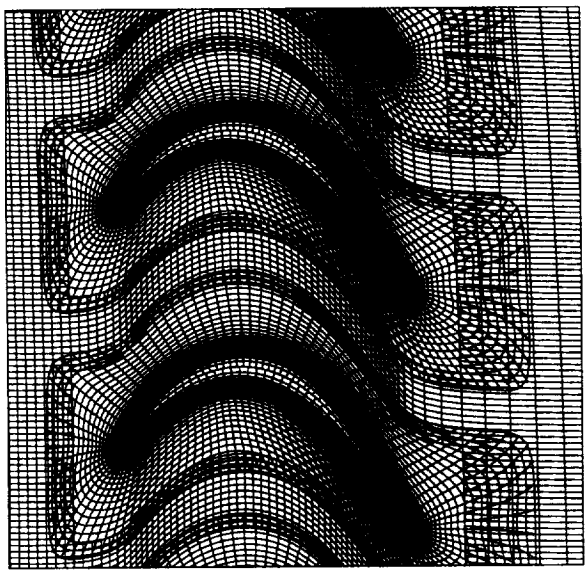

Figure 2: Radial view of rotor-2 clearance grid.

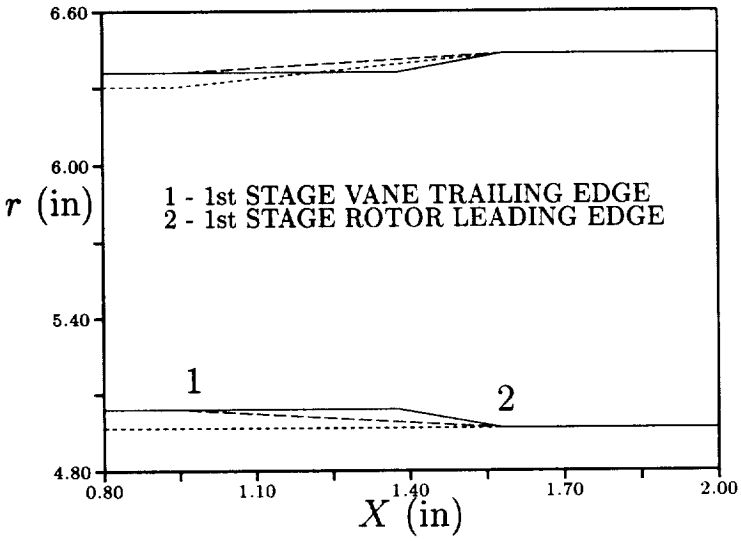

Figure 4: Endwall flowpath between first-stage vane and rotor; —— Case 1, – – Case 2, - - - Cases 3,4.

Figure 5: Instantaneous absolute Mach number contours - midspan - Case 4.

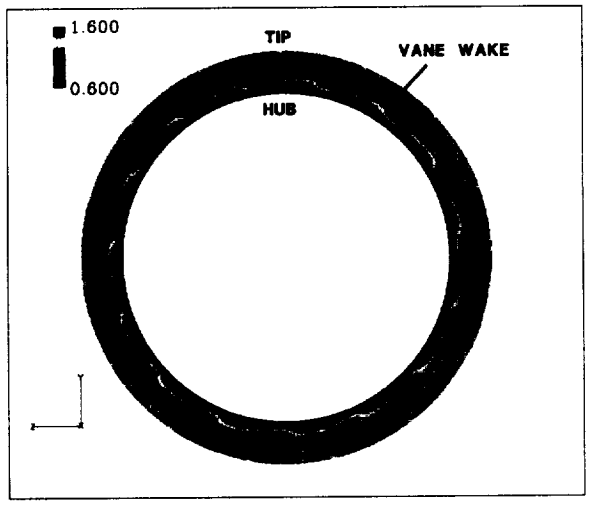

Figure 7: Time-averaged entropy contours - vane-1 exit - Case 1.

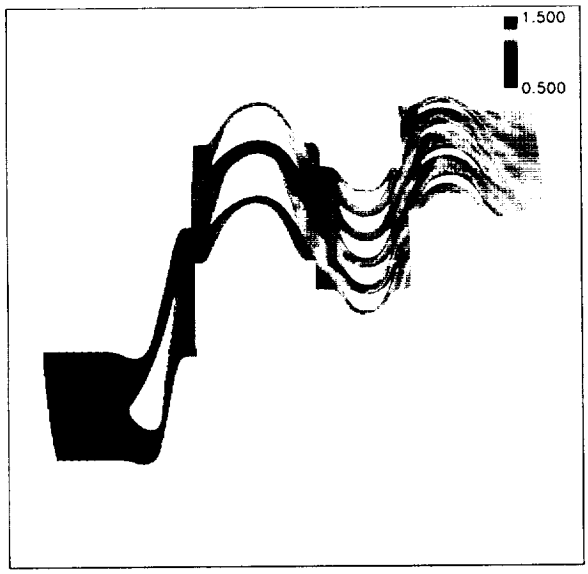

Figure 6: Instantaneous entropy contours - midspan - Case 4.

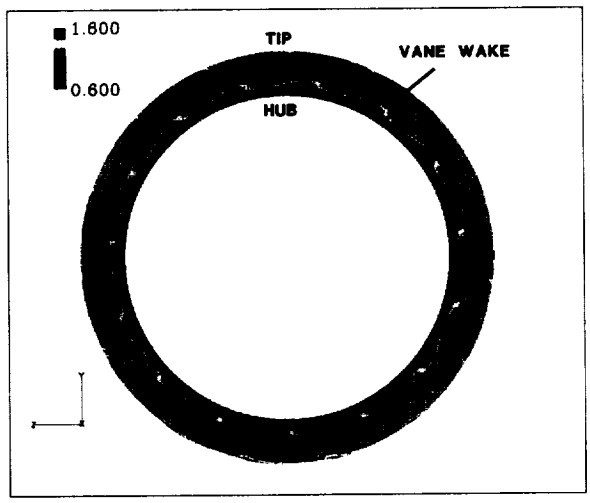

Figure 8: Time-averaged entropy contours - vane-1 exit - Case 2.

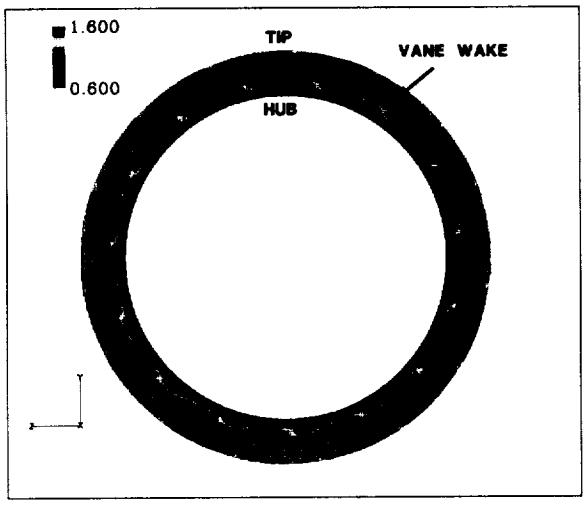

Figure 9: Time-averaged entropy contours - vane-1 exit - Case 3.

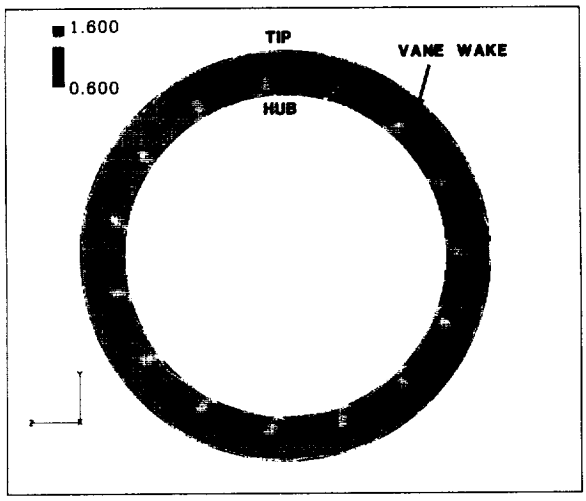

Figure 10: Time-averaged entropy contours - vane-1 exit - Case 4.

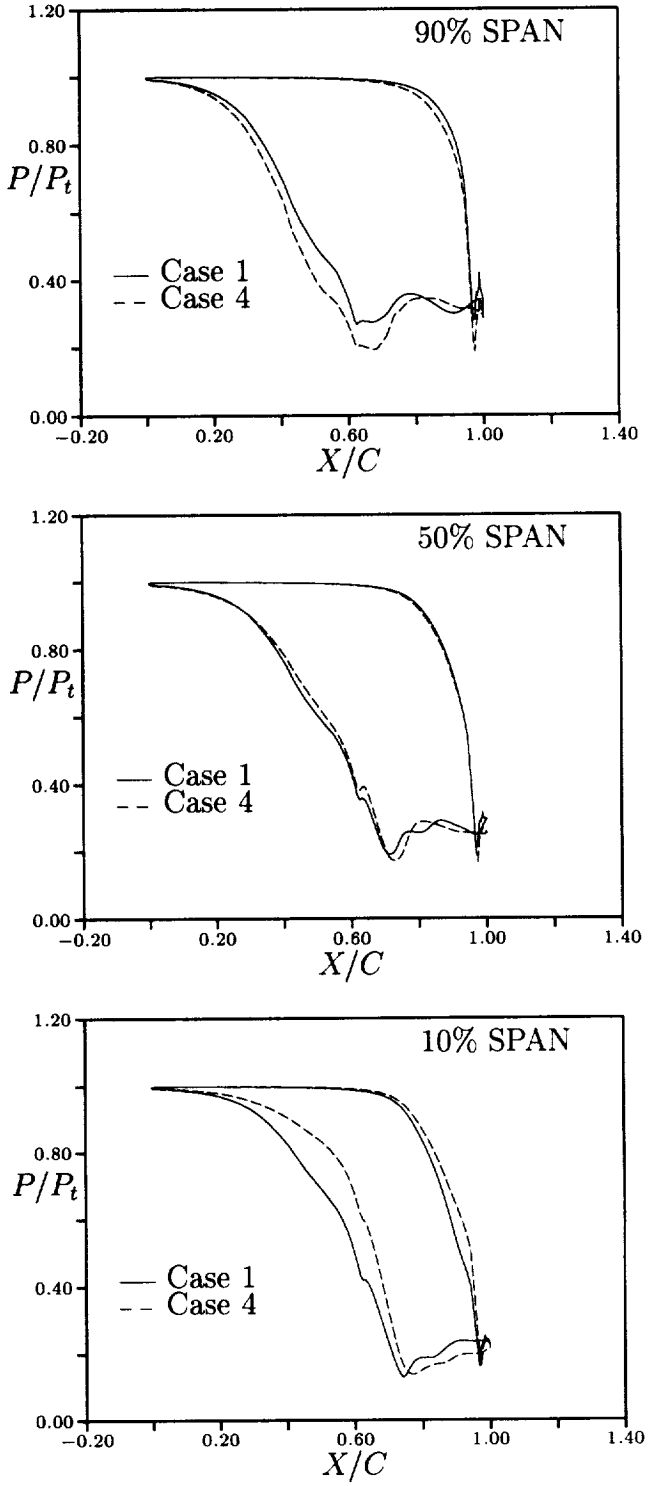

Figure 11: Time-averaged pressure - vane-1.

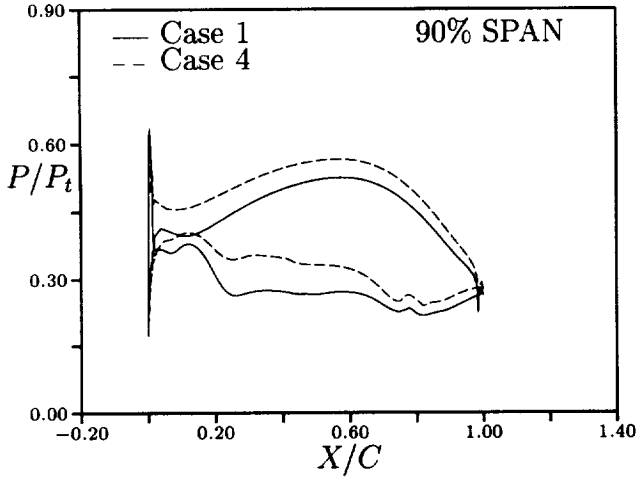

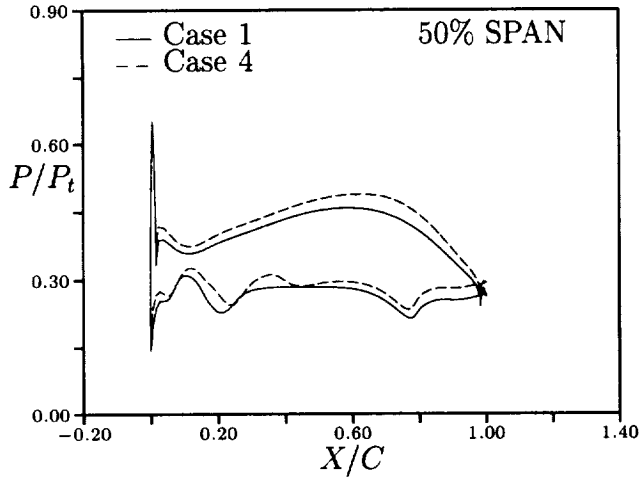

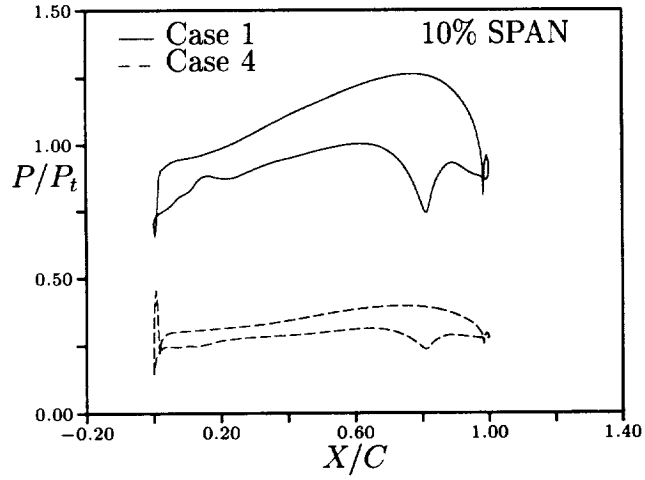

Figure 12: Time-averaged pressure - rotor-1.

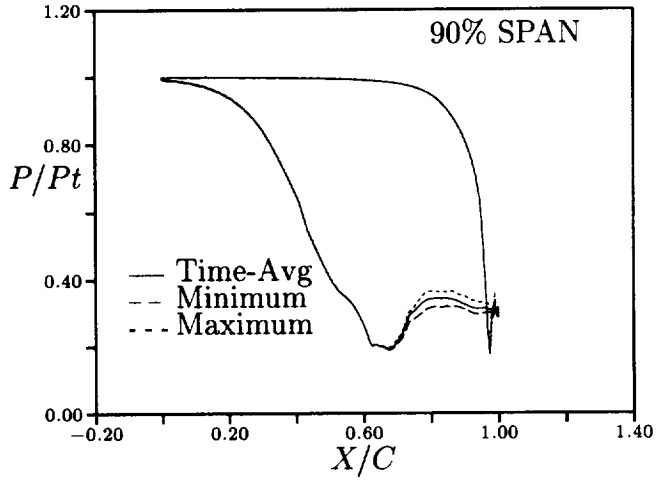

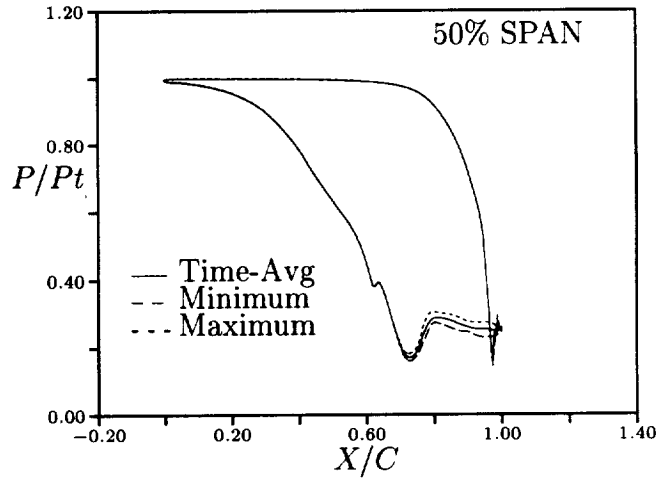

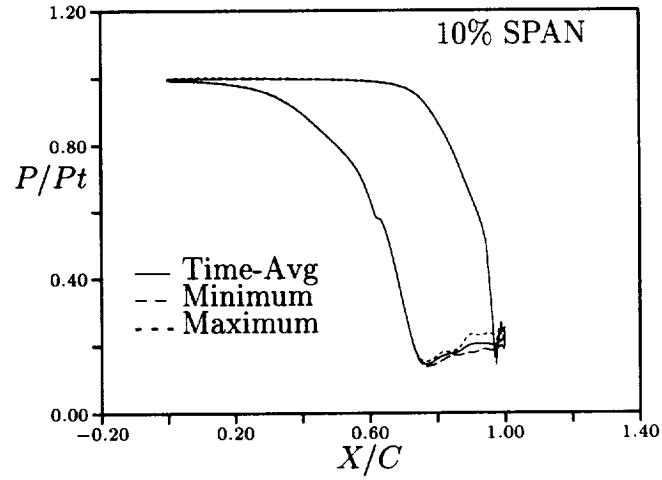

Figure 13: Pressure envelope - Case 4 - vane-1.

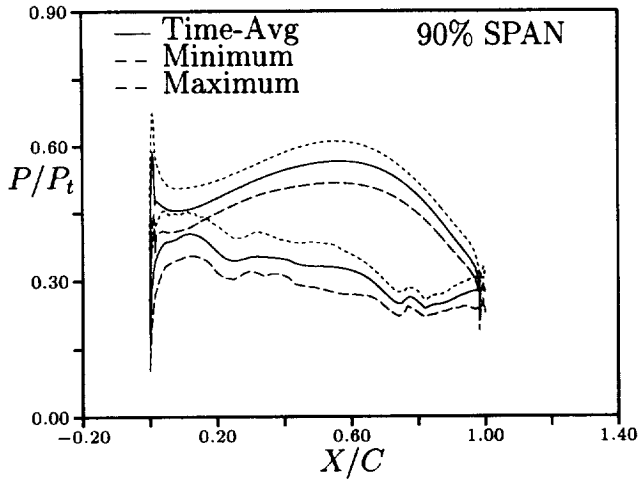

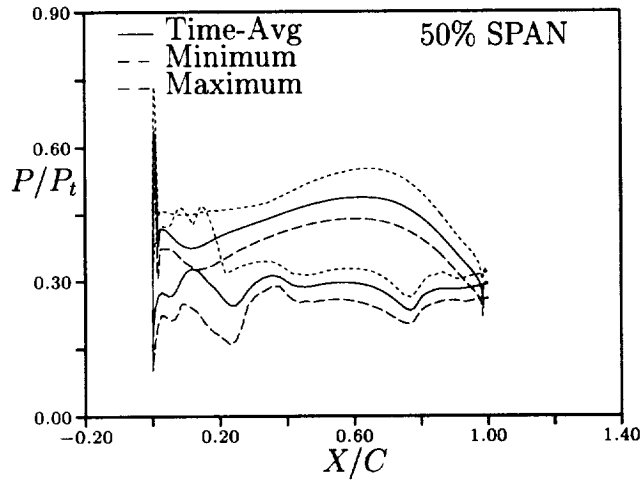

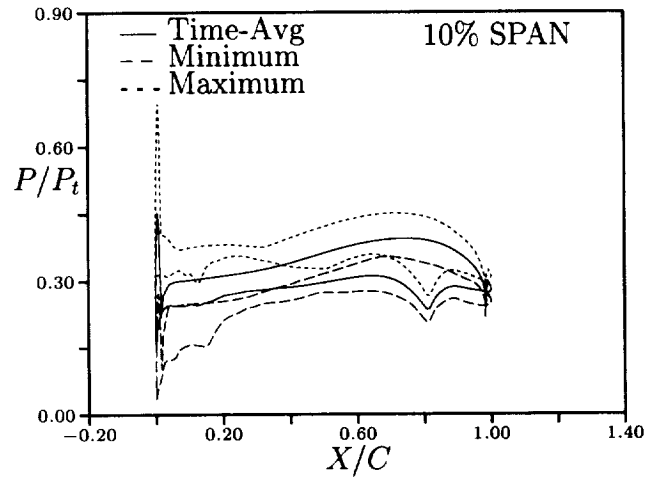

Figure 14: Pressure envelope - Case 4 - rotor-1.

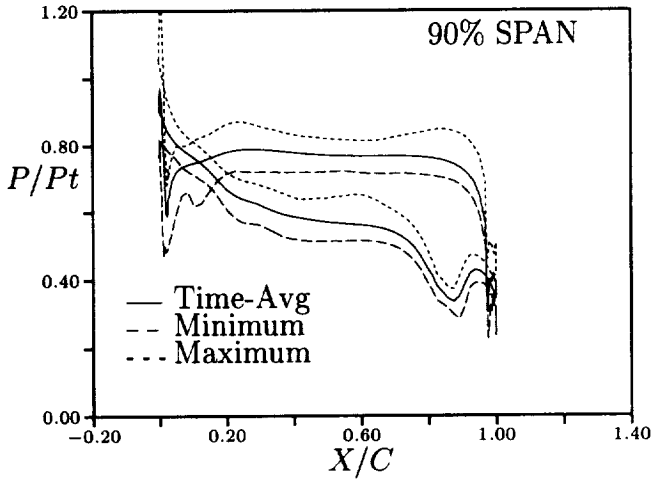

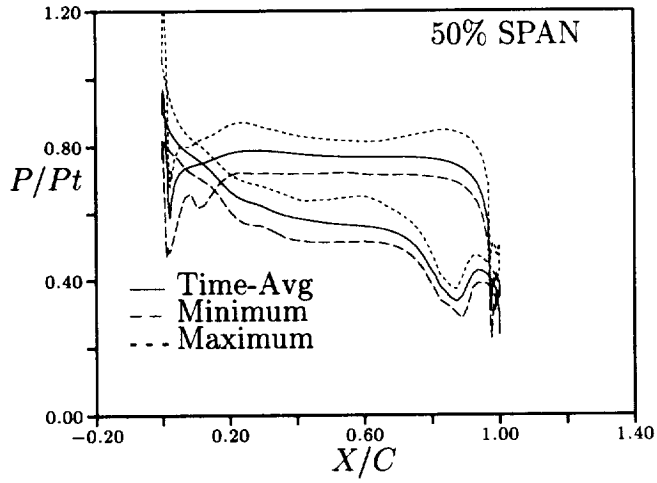

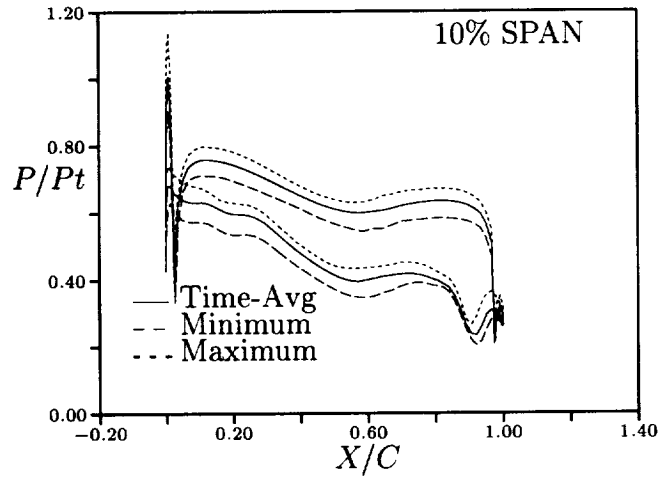

Figure 15: Pressure envelope - Case 4 - vane-2.

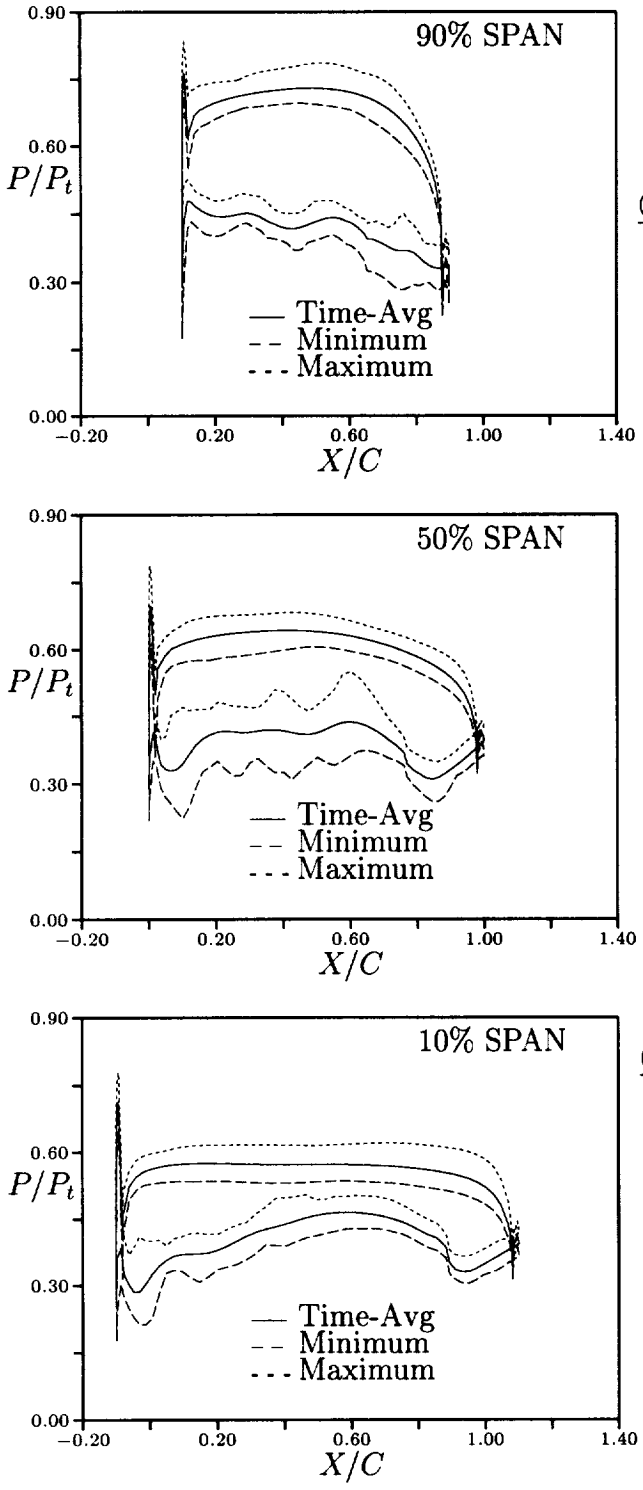

Figure 16: Pressure envelope - Case 4 - rotor-2.

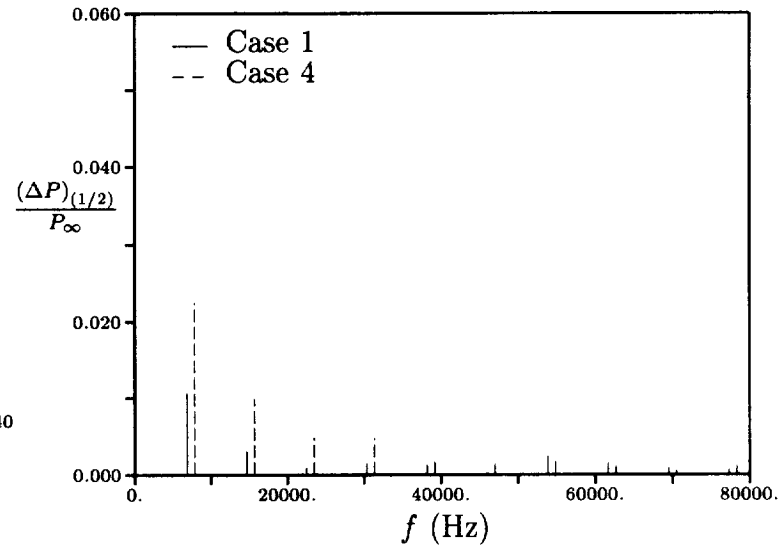

Figure 17: Fourier decomposition of unsteady pressure - rotor-1 - 5% axial chord - suction surface - 10% span.

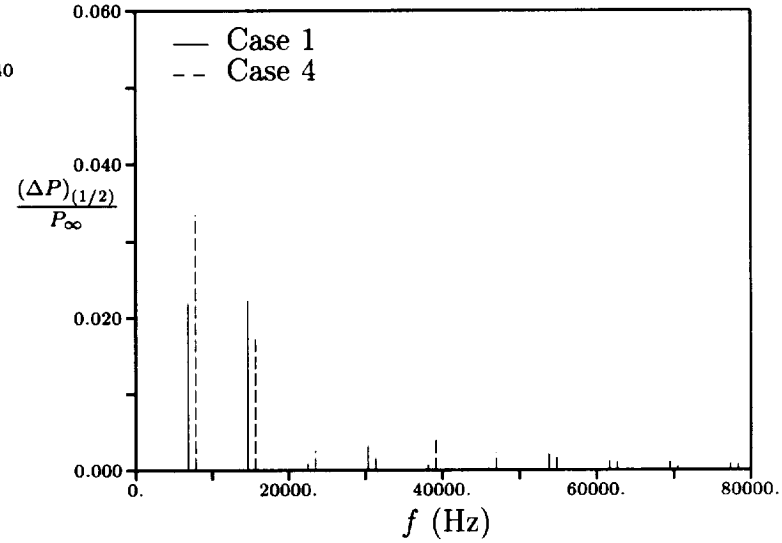

Figure 18: Fourier decomposition of unsteady pressure - rotor-1 - 5% axial chord - suction surface - 50% span.

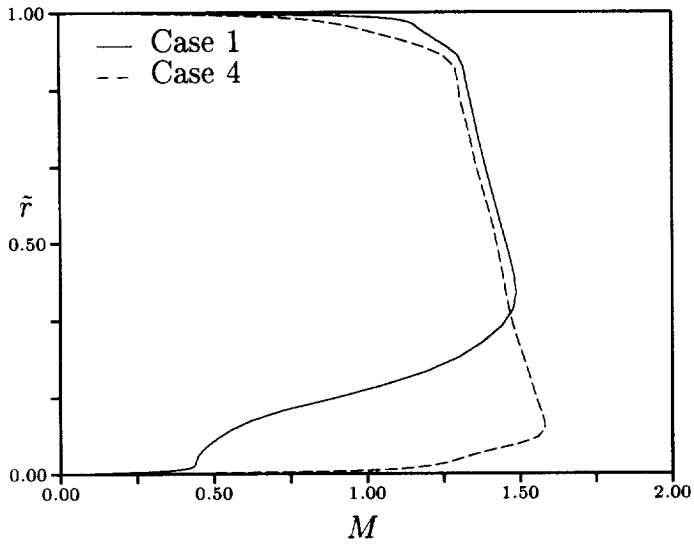

Figure 19: Absolute Mach number profile - vane-1 exit.

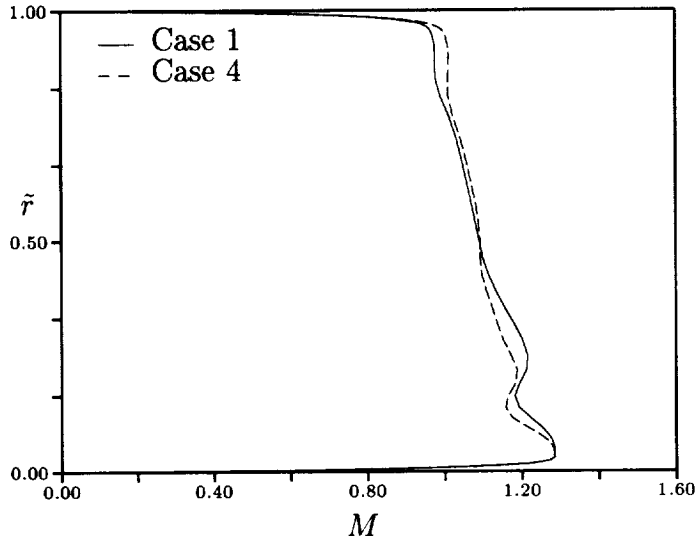

Figure 21: Absolute Mach number profile - vane-2 exit.

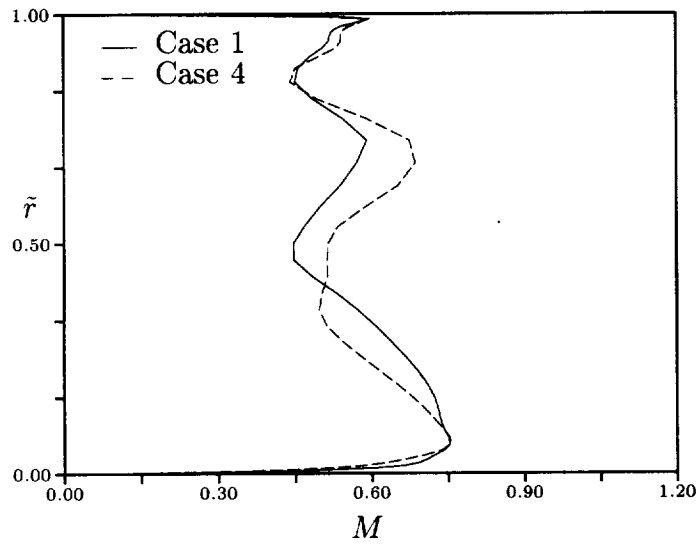

Figure 20: Absolute Mach number profile - rotor-1 exit.

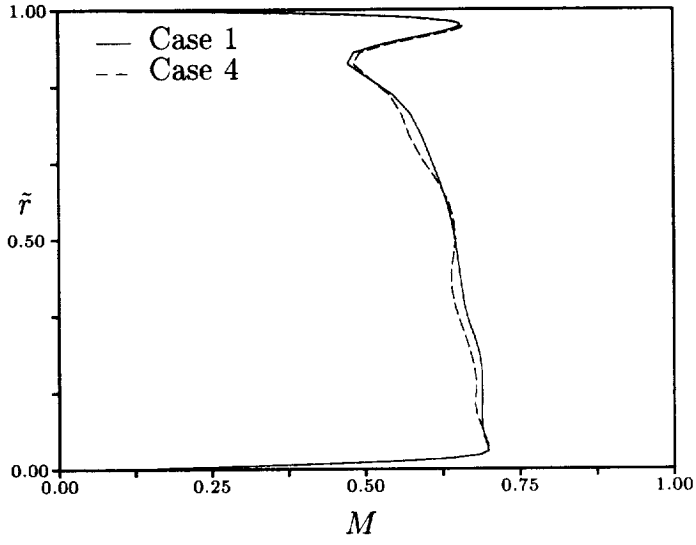

Figure 22: Absolute Mach number profile - rotor-2 exit.

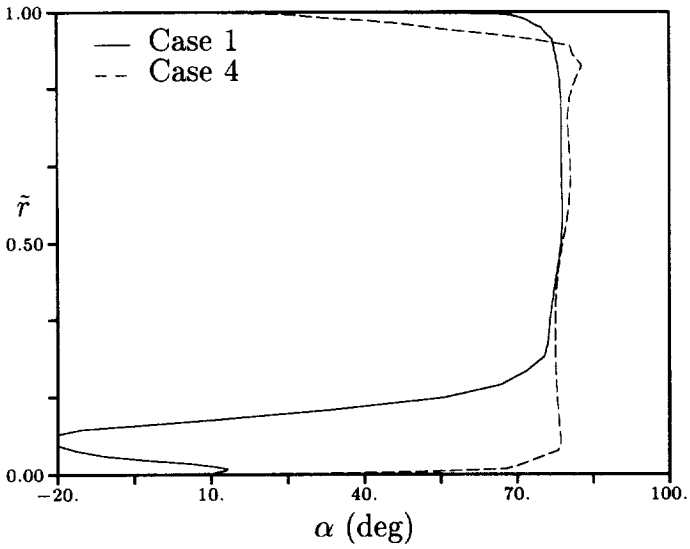

Figure 23: Absolute circumferential flow angle profile - vane-1 exit.

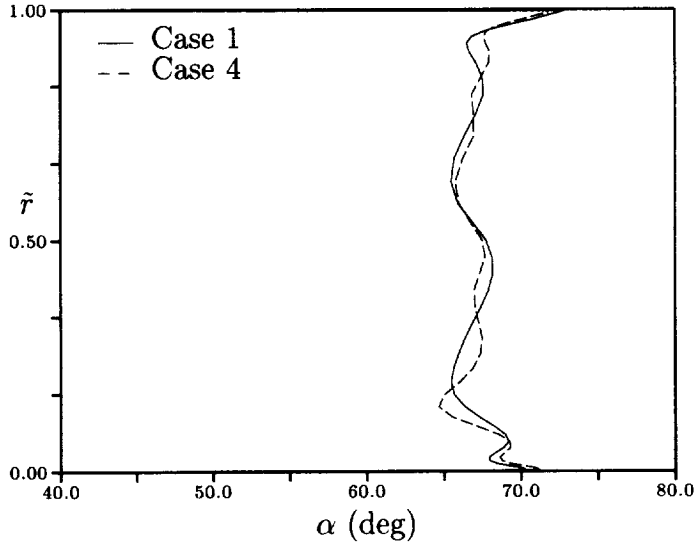

Figure 25: Absolute circumferential flow angle profile - vane-2 exit.

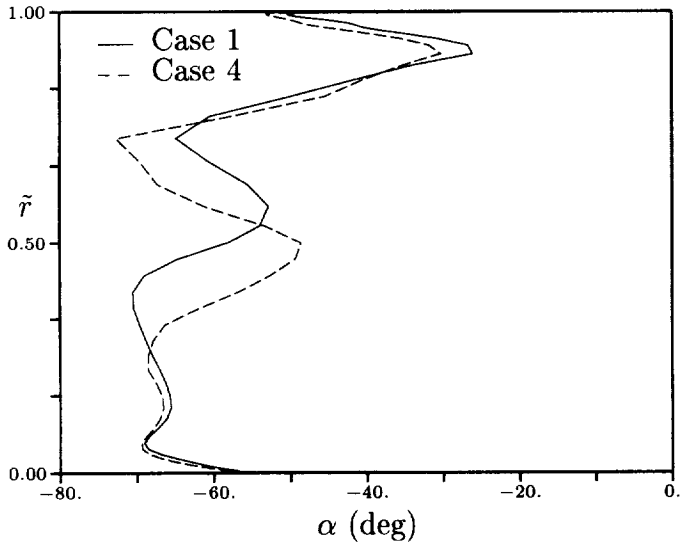

Figure 24: Absolute circumferential flow angle profile - rotor-1 exit.

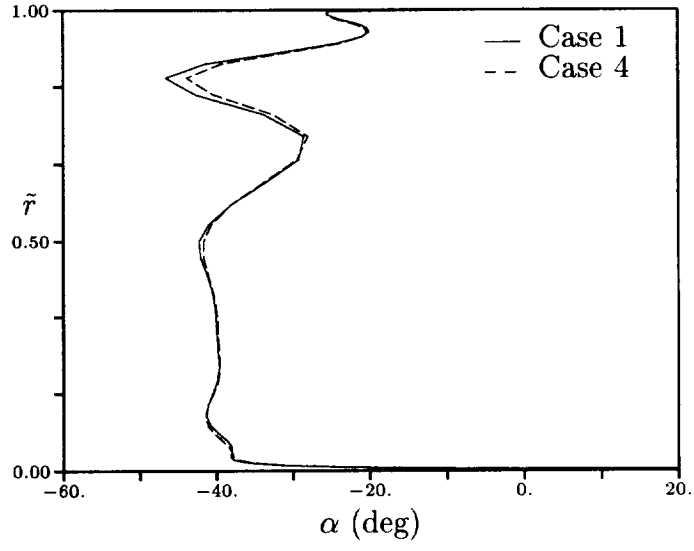

Figure 26: Absolute circumferential flow angle profile - rotor-2 exit.

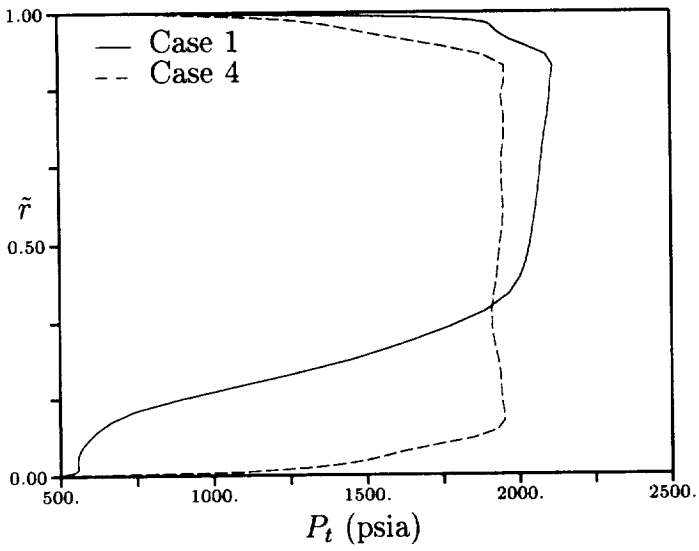

Figure 27: Absolute total pressure profile - vane-1 exit.

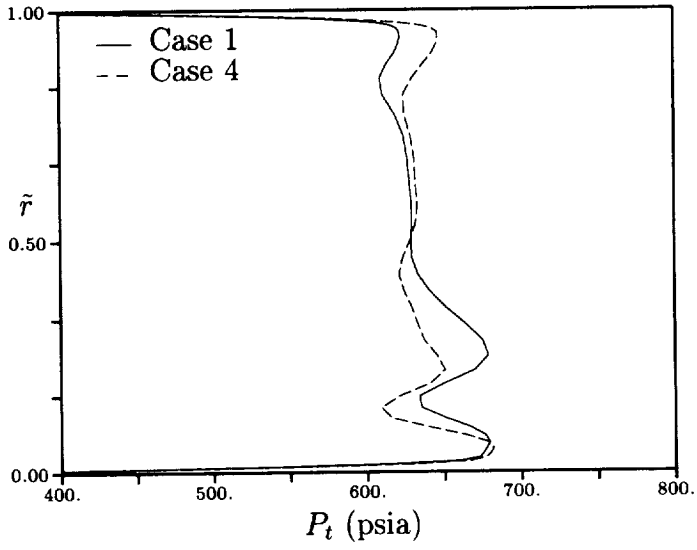

Figure 29: Absolute total pressure profile - vane-2 exit.

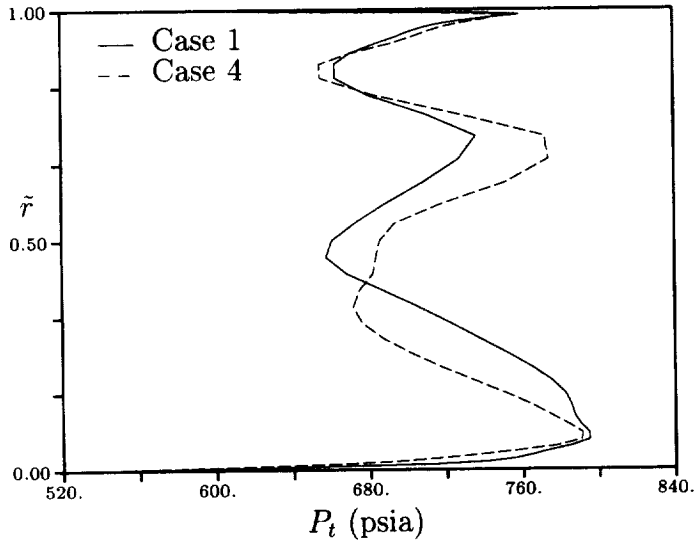

Figure 28: Absolute total pressure profile - rotor-1 exit.

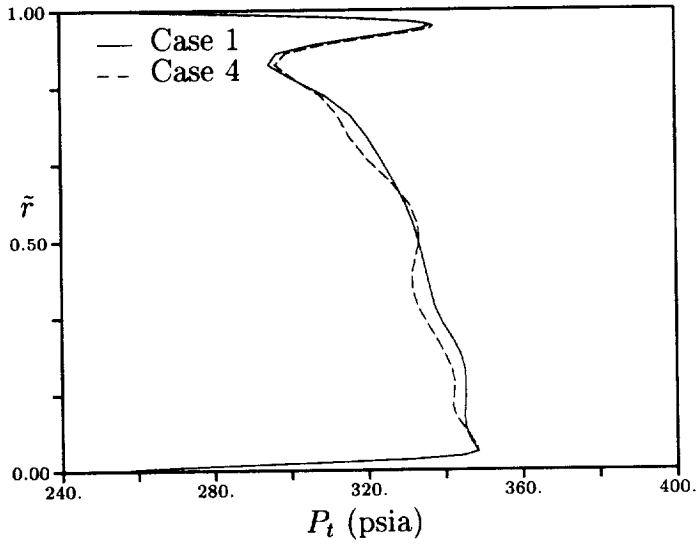

Figure 30: Absolute total pressure profile - rotor-2 exit.